RSC Advances

PAPER

Check for updates

Cite this: *RSC Adv.*, 2021, **11**, 40173

Temperature-dependent optical properties of $CuFeO_2$ through the structural phase transition†

Hsiao-Wen Chen,[a] Chu-Yun Huang,[c] Guo-Jiun Shu[bcd] and Hsiang-Lin Liu *[a]

Delafossite $CuFeO_2$ has recently attracted considerable attention because of its complex phase transitions and practical applications. A thorough understanding of the optical properties of $CuFeO_2$ is essential for its further exploration. In this paper, we investigated the temperature-dependent optical properties of $CuFeO_2$ single crystals through Raman scattering spectroscopy and spectroscopic ellipsometry. The room temperature Raman scattering spectrum exhibited six phonon modes at approximately 352, 509, 692, 1000, 1052, and 1171 cm^{-1}. Upon cooling across 11 K, which is the rhombohedral to monoclinic structural phase transition temperature, a softening of the E_g-symmetry 352 cm^{-1} mode and a hardening of the A_{1g}-symmetry 692 cm^{-1} mode were observed. Moreover, analysis of the temperature-dependent real part of the dielectric function and direct band gap revealed anomalies at 11 K. These results demonstrate a profound connection between the structural phase transition, lattice dynamics, and electronic structure of $CuFeO_2$ and provide key information for $CuFeO_2$-based device design and fabrication.

Received 4th November 2021
Accepted 9th December 2021

DOI: 10.1039/d1ra08096b

rsc.li/rsc-advances

1. Introduction

In the delafossite $CuMO_2$ (M = IIIA, transition metal elements) series, $CuFeO_2$ is a well-known p-type semiconductor.[1,2] $CuFeO_2$ has attracted attention as a p-type transparent conducting oxide that could be used for applications of anodes in lithium ion batteries.[1–3] Recent technological developments in $CuFeO_2$ and other ferrite materials have focused on the energy conversion and storage, photocatalytic degradation of pollutants in water and air, and solar fuels production *via* water splitting and CO_2 reduction.[3–9] In addition to device applications, the special magnetic structure and structural phase transition of $CuFeO_2$ are an attractive issue in fundamental science. $CuFeO_2$ has two Néel temperatures. The first Néel temperature (T_{N1}) of $CuFeO_2$ is near 16 K, where the magnetic structure is changed from paramagnetic to collinear-incommensurate antiferromagnetic without any structural phase transition. The second Néel temperature (T_{N2}) is near 11 K, where the magnetic structure is changed to collinear-commensurate antiferromagnetic without any structural phase transition. Further, the lattice structure is changed from the rhombohedral to monoclinic phase below T_{N2}.[10,11]

Numerous studies have examined the structural, magnetic, vibrational and optical properties of $CuFeO_2$. Fig. 1 illustrates the room temperature crystal structure and structural and magnetic phase transitions of $CuFeO_2$. Ye *et al.*[10] and Kimura *et al.*[11] have presented the X-ray and neutron diffraction patterns of $CuFeO_2$ powders and single crystals. At room temperature, $CuFeO_2$ has a rhombohedral structure with the $R\bar{3}m$ space group, with lattice parameters of $a = b = 3.035$ Å, $c = 17.163$ Å, $\alpha = \beta = 90°$, and $\gamma = 120°$.[10,11] In the low temperature phase, it has a monoclinic lattice structure with the $C2/m$ space group, with lattice parameters of $a = 11.574$ Å, $b = 3.040$ Å, $c = 5.982$ Å, and $\beta = 154°$.[10] The c-axis compression reduced the bond length of Cu–O from 1.83805 Å (17 K) to 1.7863 Å (4 K). The structural phase transition also induced the compression of FeO_6 octahedral units. The bond length of Fe–O was split from 2.024 Å (17 K) to 2.0225 and 2.0255 Å (4 K).[10] Temperature-dependent magnetic susceptibility revealed that the material became antiferromagnetic below $T_{N1} = 16$ K.[12] Furthermore, in neutron diffraction results, $CuFeO_2$ displayed an incommensurate antiferromagnetic structure at approximately $T_{N1} = 16$ K.[10,11] A commensurate spiral antiferromagnetic structure was exhibited at temperatures below $T_{N2} = 11$ K, and the crystal structure changed to the monoclinic phase.[10–12] The unique magnetoelectric effect of this material enables functional devices to be realized.[13–15]

Salke *et al.*[16] and Pavunny *et al.*[17] have studied the temperature-dependent Raman scattering spectra of $CuFeO_2$

[a]Department of Physics, National Taiwan Normal University, Taipei 116059, Taiwan. E-mail: hliu@ntnu.edu.tw
[b]Department of Materials and Mineral Resources Engineering, National Taipei University of Technology, Taipei 106344, Taiwan
[c]Institue of Mineral Resources Engineering, National Taipei University of Technology, Taipei 106344, Taiwan
[d]Taiwan Consortium of Emergent Crystalline Materials, Ministry of Science and Technology, Taipei 106214, Taiwan

† Electronic supplementary information (ESI) available. See DOI: 10.1039/d1ra08096b

This article is licensed under a Creative Commons Attribution-NonCommercial 3.0 Unported Licence.

© 2021 The Author(s). Published by the Royal Society of Chemistry

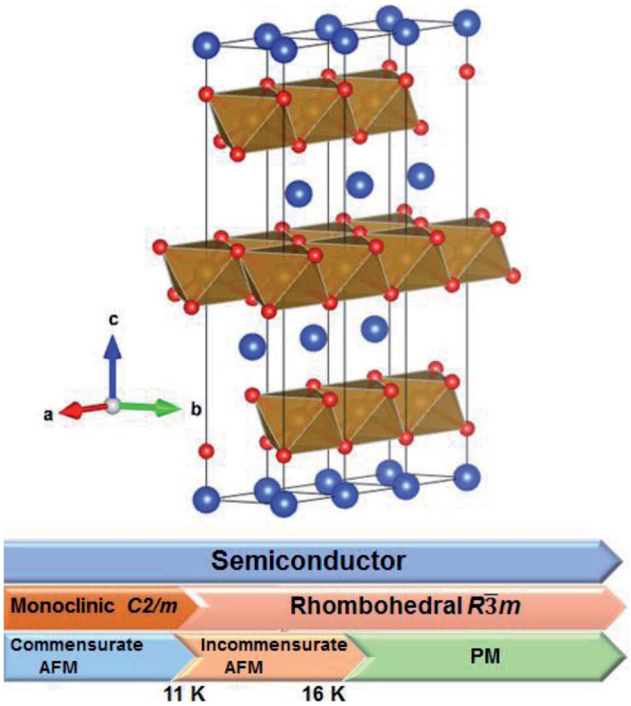

Fig. 1 Room temperature crystal structure of $CuFeO_2$ and a schematic depicting the electric, structural, and magnetic properties of $CuFeO_2$ (AFM: antiferromagnetic, and PM: paramagnetic).

single crystals and polycrystalline pellets down to the liquid nitrogen temperature. They determined that the temperature-dependent peak positions of the in-plane Fe–O vibration E_g mode and the out-of-plane Cu–O vibration A_{1g} mode could be predicted using theoretical anharmonic models. Salke *et al.*[16] further investigated the pressure-dependent Raman scattering spectra of $CuFeO_2$ single crystals up to 23 GPa. They reported that the E_g and A_{1g} modes exhibited hardening with an increase in pressure. When the pressure was higher than 18 GPa, the E_g mode split and exhibited an obvious softening, indicating a structural phase transition. Aktas *et al.*[18] presented the temperature-dependent Raman scattering spectra of $CuFeO_2$ and $CuCrO_2$ single crystals. They reported that both the E_g and A_{1g} modes exhibited a softening within 1 cm^{-1} below 14 K, which was associated with a pseudo-proper ferroelastic transition occurring in multiferroic materials. Wheatley *et al.*[19] prepared $CuFeO_2$ thin films with thickness of 21 nm and 75 nm through pulse laser deposition. Using transmittance and diffuse reflectance spectra, they found a direct band gap of approximately 1.3 to 1.4 eV at room temperature. Roble *et al.*[20] presented the room temperature diffuse reflectance spectroscopy of bulk 3R–$CuFeO_2$. They found a direct band gap of approximately 1.3 eV. Eyert *et al.*[21] reported the partial densities of states of the rhombohedral phase $CuFeO_2$. They determined that rhombohedral $CuFeO_2$ is a semiconductor with an optical band gap of 1.15 eV; the band gap value of the monoclinic $CuFeO_2$ is 0.05 eV.

Most studies have focused on room temperature optical measurements and were limited to powder samples. The temperature-dependent optical properties of $CuFeO_2$ single crystals have remained unexplored. In this study, we combined Raman scattering spectroscopy and spectroscopic ellipsometry to explore the temperature-dependent lattice dynamics and electronic structure of $CuFeO_2$ single crystals. Furthermore, we investigated the correlation between the temperature-dependent optical response of $CuFeO_2$ and its structural phase transition. Our results reveal the intricate relationship between charge-lattice interactions and structural phase transition in $CuFeO_2$.

II. Experimental methods

The single-phase $CuFeO_2$ powders were prepared by the solid-state reaction method. The starting materials used in the study were reagent-grade Cu_2O (99.9%) and Fe_2O_3 (99.9%). The $CuFeO_2$ was prepared directly from mixing Cu_2O and Fe_2O_3 in stoichiometric ratio and then calcined under N_2 atmosphere at 1123 K with following the formula of $Cu_2O + Fe_2O_3 = 2CuFeO_2$. The X-ray powder diffraction was performed to determine the phase purity of synthesized single-phase $CuFeO_2$ powders. Furthermore, the synthesized single-phase $CuFeO_2$ powders were pressed by isostatic compaction to form a cylindrical rod with 6–8 mm in diameter and 80 mm in length. We then sintered the rod at 900 °C in N_2 atmosphere with keeping 24 hours to obtain condensed rod and increase its mechanical strength. To grow the $CuFeO_2$ single crystal, we used the floating zone (FZ) method, which transfers this condensed rod into a furnace in FZ, and then crystal growth with the rate of 1 mm h^{-1} in a flow of CO/CO_2 gas. As-grown $CuFeO_2$ single crystal is opaque-black color with 5 mm in diameter and 70 mm in length. The obtained crystals in this study that formed on the (001) surface exhibited disk shapes that were 5 mm in diameter and 3 mm in thickness. The single crystals were characterized using X-ray powder diffraction and magnetization measurements.[22,23] Besides the higher cost and longer growth process, the advantages of using $CuFeO_2$ single crystal for research are high phase purity, excellent crystallinity, and easy to study the anisotropic behavior of the materials compared to $CuFeO_2$ polycrystalline powder. Moreover, X-ray powder diffraction profile revealed that the as-grown and one year aging samples exhibited almost identical pattern, implying the good stability for $CuFeO_2$.

Micro-Raman scattering measurements were performed in a backscattering geometry using a 785 nm laser. The linearly polarized light was focused into a 3 μm-diameter spot on the sample surface. The Raman scattering signal was collected and dispersed using a SENTERRA spectrometer equipped with a 1024-pixel-wide charge-coupled detector. The spectral resolution achieved using these instruments were typically less than 0.5 cm^{-1}. To avoid heating effects, the laser power was set to 0.1 mW. The polarized Raman scattering spectra were taken in scattering geometry of $\bar{Z}(YY)Z$ and $\bar{Z}(YX)Z$. In this Porto notation, the first and the last letter represent the propagation directions of the incident and the scattered light, whereas the letters in parentheses indicate the electric field polarizations of the incident and scattered light, respectively. X, Y, Z, and $\bar{Z}$ were parallel to the [100], [010], [001], and [00$\bar{1}$] crystal directions,

© 2021 The Author(s). Published by the Royal Society of Chemistry

respectively. When the polarizations of the incident and the scattered light are carefully controlled, the selection rules for the Raman scattering from phonon modes allow accurate mode assignments.[24] We placed the sample in a continuous-flow helium cryostat, which can control the temperature to be in the range of 5–300 K.[25]

Temperature-dependent spectroscopic ellipsometric spectra were obtained using a J. A. Woollam Co. M-2000U ellipsometer under a Janis ST-400 vacuum cryostat with a pressure under 10^{-8} torr. The data were collected in the spectra range between 0.73 and 6.42 eV with temperatures between 4.5 and 300 K[25,26] The raw ellipsometry variables Ψ and Δ are related to the complex Fresnel reflection coefficients for light polarized parallel (R_p) and perpendicular (R_s) to the plane of incidence.

$$\tan \Psi e^{i\Delta} = \frac{R_p}{R_s} \quad (1)$$

For isotropic bulk materials, the dielectric function can be transformed by the raw ellipsometry variables Ψ and Δ. However, the surface roughness would cause a small absorption below the absorption edge.[27] The complex dielectric function was determined from fitting the ellipsometric variables by building a three medium optical model consisting of an air ambient structure/surface roughness/single crystal.[25,26] The surface roughness can be described by a Bruggeman effective medium approximation by assuming 50% vacuum and 50% bulk.[28] The surface roughness was approximately 1 nm in $CuFeO_2$.

III. Results and discussion

A. Vibrational properties

The room temperature polarized Raman scattering spectra of $CuFeO_2$ are presented in Fig. 2. Polarized Raman scattering studies allow one to obtain the symmetry properties and assignments of different Raman-active phonon modes. In the $\bar{Z}(YY)Z$ configuration, we observed two main peaks at approximately 352 and 692 cm^{-1}. In addition, a broad peak was observed at approximately 509 cm^{-1}, which was attributed to the Cu vacancy induced phonon mode.[16] We also observed low-intensity broad phonon modes near 1000, 1052, and 1171 cm^{-1}, which should be ascribed to multiphonon bands.[29–31] According to factor group analysis, $CuFeO_2$ has a rhombohedral structure (space group $R\bar{3}m$) containing one formula unit per primitive cell. The irreducible representation of the phonon modes at the center of the Brillouin zone is given by $\Gamma = A_{1g} + E_g + 3A_{2u} + 3E_u$.[16] These modes were classified as Raman active ($A_{1g} + E_g$), infrared active ($2A_{2u} + 2E_u$), and acoustic ($A_{2u} + E_u$). In the $\bar{Z}(YX)Z$ configuration, the intensity of the 352 cm^{-1} mode became much stronger than that in the $\bar{Z}(YY)Z$ configuration, indicating that it is of the E_g character.[12–14] By contract, the 692 cm^{-1} and multiphonon modes almost vanished, indicating that they exhibit A_{1g} symmetry.[16–18] Our room temperature experimental results are consistent with those of previous studies.[16–18]

The temperature-dependent unpolarized Raman scattering spectra of $CuFeO_2$ are depicted in Fig. 3. With a decrease in temperature, the peak positions of all phonon modes shifted to higher frequencies, their resonance linewidth narrowed, and their intensity increased. Six Lorentzian oscillators were used to fit the Raman scattering spectrum at 5 K (inset of Fig. 3). Fig. 4 illustrates the frequencies, linewidths, and normalized intensities of the E_g and A_{1g} phonon modes as a function of temperature. The oscillation strength of the E_g and A_{1g} phonon modes increased as temperature decreased, but remained constant when the temperature was lower than 100 K. In a normal anharmonic solid, when temperature decreases, the

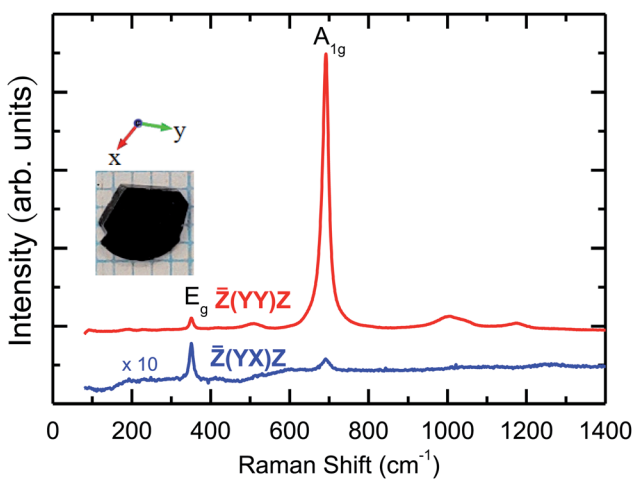

Fig. 2 The room temperature polarized Raman scattering spectra of $CuFeO_2$ and the optical image of $CuFeO_2$. The notations used for the crystallographic directions are also given.

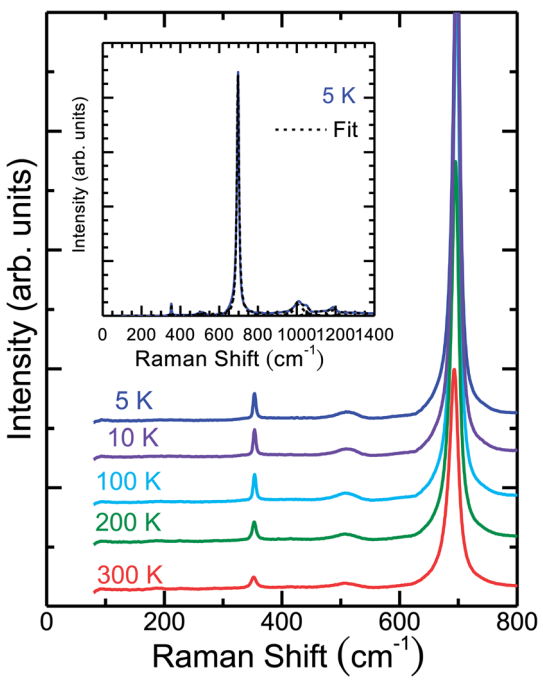

Fig. 3 Temperature-dependent unpolarized Raman spectra of $CuFeO_2$. The inset illustrates the fitting results of spectra obtained at 5 K using the Lorentzian model.

© 2021 The Author(s). Published by the Royal Society of Chemistry

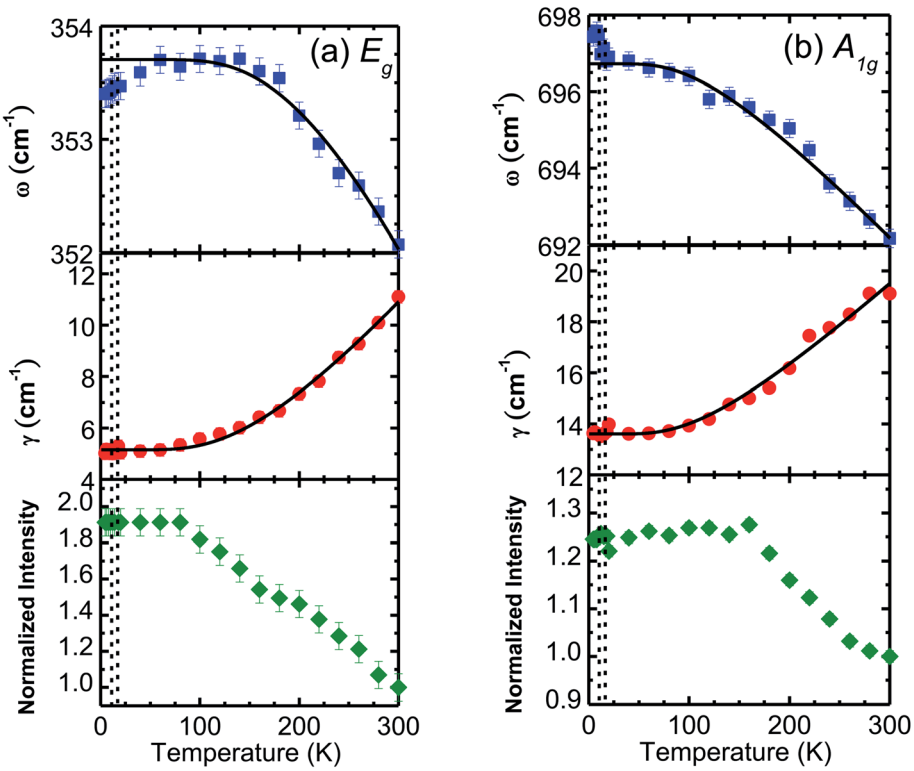

Fig. 4 Temperature-dependent frequency, linewidth, and normalized intensity of the (a) E_g and (b) A_{1g} phonon modes of $CuFeO_2$. The fitting results of the anharmonic model are represented in the solid lines. The vertical dashed lines denote the phase transition temperatures at 11 and 16 K.

phonon frequency should increase and linewidth decrease. The temperature-dependent phonon frequency and linewidth can be written as[32]

$$\omega(T) = \omega_O + A\left[1 + \frac{2}{\exp(\Theta/T) - 1}\right] \quad (2)$$

and

$$\gamma(T) = \gamma_O + B\left[1 + \frac{2}{\exp(\Theta/T) - 1}\right] \quad (3)$$

where Θ is the Debye temperature and ω_o and γ_o are the frequency of the optical phonon mode and the linewidth at 0 K, respectively.[32] The parameters A and B are the anharmonic coefficients. The values of ω_o ($\approx$353.7 cm^{-1}), γ_o ($\approx$5.2 cm^{-1}), A (≈ -6.0 cm^{-1}), and B ($\approx$4.6 cm^{-1}) were determined to analyze the anharmonic contributions to the 352 cm^{-1} E_g mode. For the 692 cm^{-1} A_{1g} mode, the values of ω_o ($\approx$696.7 cm^{-1}), γ_o ($\approx$14 cm^{-1}), A (≈ -1.4 cm^{-1}), and B ($\approx$9.6 cm^{-1}) were determined. The average Debye temperature was 357 K, which was lower than that of other delafossite materials ($CuCrO_2$, Θ = 830 K).[33] Parameter A was negative, indicating that the peak frequency shifted higher as temperature decreased. By contrast, parameter B was positive, indicating that the linewidth became narrower as temperature decreased. Theoretical predictions based on eqn (2) and (3) are the solid lines in Fig. 4(a) and (b). Fig. S1† presents the temperature-dependent Raman scattering spectra of the multiphonon modes of $CuFeO_2$. Fig. S2† further displays the frequency, damping, and normalized intensity of the multiphonon modes as a function of temperature. As temperature decreased, the phonon frequency exhibited hardening and the linewidth narrowed. The temperature-dependent variation of all phonon frequencies and linewidths can be fit well using the anharmonic model.

When the temperature was below 11 K, which was denoted as structural phase transition in Fig. 1, the E_g mode exhibited a softening and the A_{1g} mode exhibited a hardening. Our results differ from those of the previous studies, in which both the E_g and A_{1g} modes exhibited a redshift below 14 K.[18] Previous neutron diffraction studies indicated that the lattice constant a of the monoclinic phase was nearly three times larger than that of rhombohedral phase, whereas the lattice constant b remained almost the same. By contrast, the lattice constant c of the monoclinic phase was two times smaller than that of the rhombohedral phase.[10] The E_g mode exhibited a softening with a 0.9 cm^{-1} deviation from the theoretical predictions of the anharmonic model. By contrast, the A_{1g} mode exhibited a hardening with a 0.8 cm^{-1} deviation from the theoretical predictions of the anharmonic model. The effects of the structural phase transition in $CuFeO_2$ caused in-plane vibration softening and out-of plane vibration hardening.

© 2021 The Author(s). Published by the Royal Society of Chemistry

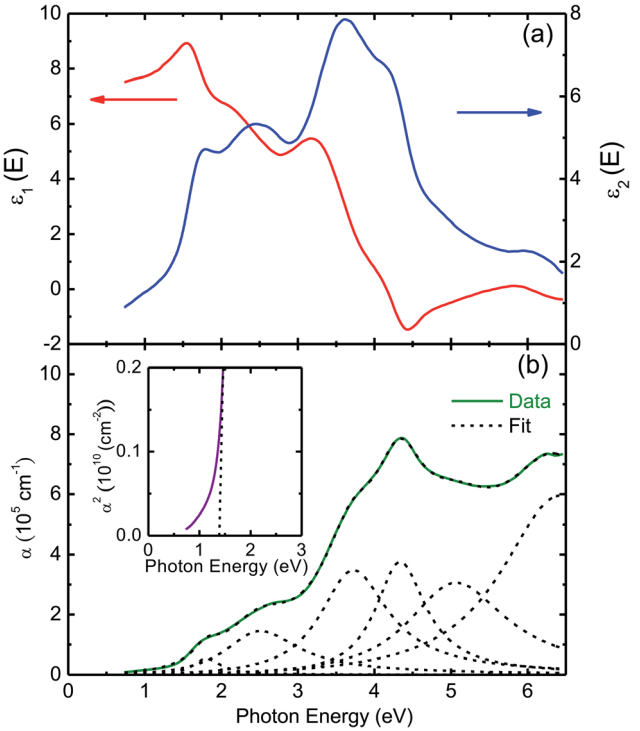

Fig. 5 (a) The complex dielectric function of $CuFeO_2$ at room temperature. (b) Room temperature optical absorption coefficient spectrum of $CuFeO_2$. The dashed lines are the fitting results using the Lorentzian model. The inset illustrates the direct band gap analysis of CuFeO2 at 300 K.

B. Electronic excitations

Fig. 5(a) presents the room temperature real ε_1 and imaginary ε_2 parts of the dielectric function $\varepsilon(\omega)$ of $CuFeO_2$ through ellipsometric analysis. The room temperature experimental ellipsometric and best-fit calculated data of $CuFeO_2$ are presented in Fig. S3.† The dispersion response of the frequency-dependent ε_1 is typical of a semiconductor. Optical transitions are identified in the spectra according to resonance and antiresonance features that appeared at the same energy in ε_1 and ε_2, respectively. Specifically, the imaginary part spectrum ε_2 of $CuFeO_2$ was dominated by several optical transitions. Fig. 5(b) illustrates the room temperature optical absorption coefficient spectrum of $CuFeO_2$. We calculated the optical absorption coefficient using the equation $\alpha = \frac{2\omega}{c}\sqrt{\frac{1}{2}\sqrt{(\varepsilon_1(\omega)^2+\varepsilon_2(\omega)^2)}-\varepsilon_1(\omega)^2}$. The optical absorption spectrum was modeled reasonably well using the Lorentzian oscillator. Optical absorption started to gradually increase above 0.7 eV, reached a maximum value at approximately 4.3 eV, and then leveled off. The first absorption peak near 1.76 eV was assigned to the on-site iron ion 3d t_{2g} to 3d e_g transition. The second absorption peak near 2.51 eV was assigned to the copper 3d to iron 3d e_g transition. The absorption peaks at approximately 3.70, 4.33, and 5.06 eV were associated with the charge-transfer transitions from the 2p orbital of oxygen to the 3d orbital of copper or iron.[20] In a normal solid, the optical absorption coefficient $\alpha(E)$ includes contributions from both direct and indirect band gap transitions.[34] The optical absorption coefficient is given by

$$\alpha(E) = A\left(E - E_{g,dir}\right)^{0.5} + B\left(E - E_{g,indir} \mp E_{ph}\right)^2 \quad (4)$$

where $E_{g,dir}$ and $E_{g,ind}$ are the magnitudes of the direct and indirect gaps, respectively; E_{ph} is the emitted (absorbed) phonon energy; and A and B are constants. This model, which assumes a simple band shape, enables the extraction of the direct energy gap when α^2 is plotted as a function of photon energy. The inset of Fig. 5(b) illustrates the direct band gap of 1.43 ± 0.01 eV. Our result is similar to that of previous UV-Vis absorption spectrum analyses and theoretical calculations.[18–20] To confirm that the $CuFeO_2$ single crystal is a direct band gap material, Fig. S4† presents the room temperature photoluminescence spectrum of $CuFeO_2$ determined using a 325 nm excitation laser. The strong photoluminescence signal at approximately 1.3 eV indicated that $CuFeO_2$ has a direct band gap.

Fig. 6(a) and (b) depict the temperature-dependent complex dielectric function of $CuFeO_2$. When temperature decreased, the real part ε_1 decreased in the near-infrared region. Additionally, the real part dielectric function at 1 eV was discontinuous below 11 K. A discontinuous dielectric function due to

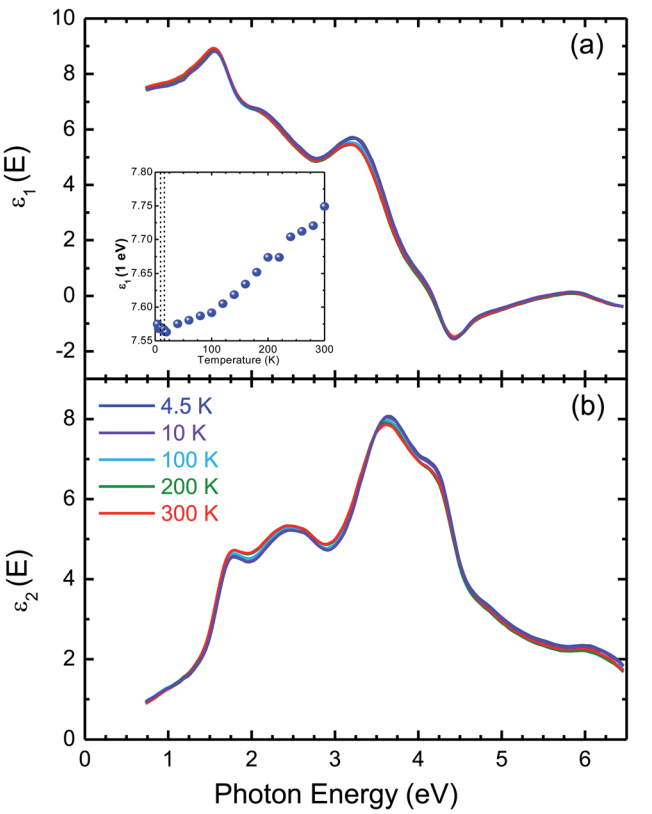

Fig. 6 Temperature dependence of (a) the real and (b) imaginary parts of the dielectric function of $CuFeO_2$. The inset highlights the temperature-dependent real part of the dielectric function at 1 eV. The vertical dashed lines denote the phase transition temperatures at 11 and 16 K.

© 2021 The Author(s). Published by the Royal Society of Chemistry

a structural phase transition has been observed in transition metal oxides, such as $BaTiO_3$.[35] When temperature decreased, the intensity of the imaginary part ε_2 slightly increased at photon energies higher than 3 eV. By contrast, the intensity slightly decreased at photon energies lower than 3 eV. The optical transition peaks at approximately 2.5 and 3.7 eV exhibited a blueshift with decreasing temperature.

The temperature-dependent optical absorption coefficient spectra are presented in Fig. 7. The inset of Fig. 7 highlights the temperature-dependent band gap energy. The band gap became higher when temperature decreased. The band gap of typical inorganic semiconductors as a function of temperature can effectively be described in terms of the Bose–Einstein model[36]

$$E_g(T) = E_g(0) - \frac{2a_B}{\exp(\Theta_B/T) - 1} \quad (5)$$

where $E_g(0)$ is the band gap energy at 0 K, a_B is the intensity of the phonon–electron interactions, and Θ_B is the average phonon temperature. Our fitting results indicated that the band gap at 0 K should be 1.43 eV. The parameters a_B and Θ_B were 6 meV and 273 K, respectively. These fitting results are similar to those of other multiferroic oxides, such as $BiFeO_3$.[37,38] As is evident from the inset of Fig. 7, the Bose–Einstein model satisfactorily reproduced the overall temperature-dependent band gap in $CuFeO_2$. Notably, the band gap deviated from the theoretical predictions of the Bose–Einstein model below 11 K. The band gap exhibited a softening of 2 meV. A similar discontinuous shift behavior has been observed in other oxide materials, such as $SrTiO_3$ (ref. 39) and $PbTiO_3$.[40] In the monoclinic phase, the first-principles calculation predicted the band gap value is 0.05 eV.[21] This small band gap indicated that the absorption edge of $CuFeO_2$ should exhibit a large redshift below 11 K. By contrast, the experimental results did not reveal any significant difference in the absorption edge across the structural phase transition. Future experimental work will concentrate on the far-infrared studies of $CuFeO_2$.

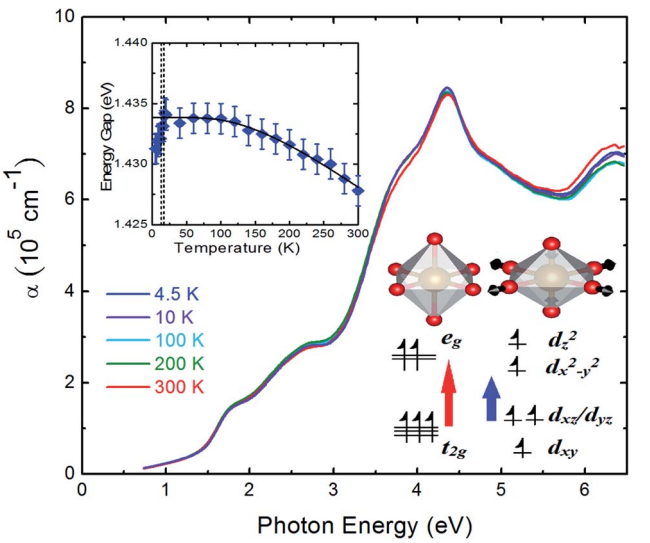

Fig. 7 Temperature-dependent optical absorption coefficient spectra of $CuFeO_2$. The inset illustrates the temperature-dependent band gap energy. The solid line is the fitting result using the Bose–Einstein model. The vertical dashed lines denote the phase transition temperatures at 11 and 16 K. The inset presents the Jahn–Teller distortion of FeO_6 octahedral unit and a schematic energy level diagram for the electronic states of Fe^{3+} ions.

The inset of Fig. 7 illustrates an energy level diagram for the electronic states of Fe^{3+} ions. In the high temperature rhombohedral phase, non-distorted FeO_6 octahedral units led to the splitting of Fe^{3+} d^5 electronic orbitals to lower t_{2g} energy levels and higher e_g energy levels because of the crystal field effect of octahedral structure. The Fe 3d t_{2g}, O 2p, and Cu 3d orbitals comprised the highest valence band states. The Fe 3d e_g, and Cu 4s orbitals comprised the lowest conduction band states.[21] For the high spin state ($S = 5/2$) of Fe^{3+} ions, all electrons occupied the Fe 3d orbital evenly. The red arrow in the inset of Fig. 7 indicates that the band gap is the electronic excitation from the Fe 3d t_{2g} to Fe 3d e_g levels. In the low temperature monoclinic phase, the compression of the *c*-axis lattice constant and the elongation of the *ab*-plane due to the structural phase transition resulted in the distortions of the FeO_6 octahedral unit.[10] From the rhombohedral to monoclinic phase, the bond length of Fe–O in the FeO_6 octahedral unit was split into two values.[10] The in-plane bond length of Fe–O increased. By contrast, the out-of-plane bond length of Fe–O decreased. This Jahn–Teller distortion of FeO_6 octahedral unit occurred in other iron oxides as well.[41] The compression of the FeO_6 octahedral unit led to the t_{2g} energy level splitting to a lower d_{xy} energy level and a higher d_{xz}/d_{yz} energy level. The elongation of the *ab*-plane led to e_g energy splitting to a lower $d_{x^2-y^2}$ energy level and a higher d_{z^2} energy level. The blue arrow in the inset of Fig. 7 indicates that the band gap is the electronic excitation from the Fe d_{xz}/d_{yz} to Fe $d_{x^2-y^2}$ levels. Under the Jahn–Teller distortion, the band gap decreased, which was in good agreement with the observed band gap redshift below 11 K.

To gain further insight into the electronic structure of $CuFeO_2$, we plotted the temperature-dependent peak position, linewidth, and normalized intensity of the optical transitions as 1.76 and 4.33 eV in Fig. 8. We also used the Bose–Einstein model to describe the temperature-dependent optical absorption peak energy and linewidth[42]

$$E = a - b\left[1 + \frac{2}{e^{\frac{\Theta}{T}} - 1}\right] \quad (6)$$

and

$$\Gamma = \Gamma_o\left[1 + \frac{2}{e^{\frac{\Theta}{T}} - 1}\right] + \Gamma_1 \quad (7)$$

where Γ_1 and a are the linewidth and transition energy at 0 K, respectively, b and Γ_o represent the strength of the electron–phonon interactions, and Θ is the average phonon temperature. By analyzing the d–d electronic excitation at 1.76 eV, we

© 2021 The Author(s). Published by the Royal Society of Chemistry

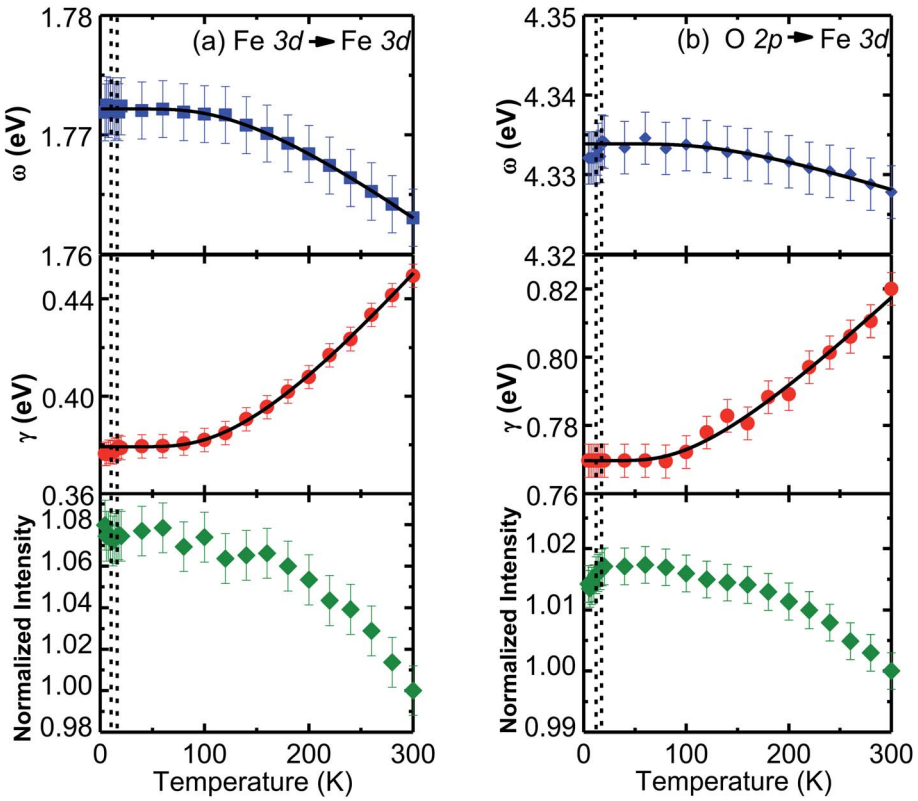

Fig. 8 Temperature-dependent peak energy, linewidth, and normalized intensity of (a) 1.76 and (b) 4.33 eV optical transitions. The fitting results of the Bose–Einstein model are represented in the solid lines. The vertical dashed lines denote the phase transition temperatures at 11 and 16 K.

determined the values of a ($\approx$1.77 eV), b ($\approx$30 meV), Γ_1 ($\approx$0.38 eV), Γ_o ($\approx$0.12 eV), and Θ ($\approx$441 K). By analyzing the charge transfer excitation at 4.33 eV, we determined the values of a ($\approx$4.33 eV), b ($\approx$5 meV), Γ_1 ($\approx$0.77 eV), Γ_o ($\approx$0.14 eV), and Θ ($\approx$450 K). Theoretical predictions based on eqn (6) and (7) are represented by the solid lines in Fig. 8(a) and (b). The peak position and linewidth of 1.76 eV optical transition followed the predictions of the Bose–Einstein model with no anomalies across the structural phase transition temperature, indicating that the charge-lattice coupling was too weak to be observed for this electronic excitation. Notably, the peak position of 4.33 eV optical transition differed slightly from the Bose–Einstein model below 11 K as a result of the structural phase transition.

IV. Summary

We investigated the temperature-dependent optical properties of $CuFeO_2$ single crystals using Raman scattering spectroscopy and spectroscopic ellipsometry. We focused on the correlation between the temperature-dependent optical response of $CuFeO_2$ and its structural phase transition. The E_g Raman-active phonon mode exhibited a redshift whereas the A_{1g} Raman-active phonon mode exhibited a blueshift across the structural phase transition at 11 K. The temperature-dependent real part of dielectric function and the direct band gap presented anomalies at 11 K. These results suggest that the onset of the structural phase transition alters the character of local atomic displacements and electronic states of FeO_6 octahedral unit and therefore induces changes in lattice dynamics and electronic structure of $CuFeO_2$. The results of this study provide valuable information for $CuFeO_2$-based device design and fabrication.

Data availability statement

The data that support the findings of this study are available from the corresponding author upon reasonable request.

Author contributions

H. L. L. and G. J. S. conceived the research and was responsible for the experimental design. H. W. C. conducted the experiments. C. Y. H. and G. J. S. were responsible for the sample preparation. H. W. C. and H. L. L. drafted the paper. All contributing authors have discussed the results and provided their comments regarding the manuscript.

Conflicts of interest

The authors declare no competing interests.

Acknowledgements

H. L. L. thanks the Ministry of Science and Technology of the Republic of China for its financial support under Grants No.

© 2021 The Author(s). Published by the Royal Society of Chemistry

MOST 110-2112-M-003-017. G. J. S. thanks financial support from the Ministry of Science and Technology of Republic of China under Grants No. MOST 108-2112-M-027-002-MY3 and 110-2124-M-002-019. H. W. C. and H. L. L. specially thanks Y. T. L. and F. Y. L. for helping the photoluminescence measurements.

References

1 Y. Dong, C. Cao, Y. S. Chui and J. A. Zapien, Facile hydrothermal synthesis of $CuFeO_2$ hexagonal platelets/rings and grapheme composites as anode materials for lithium ion batteries, *Chem. Commun.*, 2014, **50**, 10151.

2 J. Patzsch, I. Balog, P. Krau, C. W. Lehmann and J. J. Schneider, Synthesis, characterization and p–n type gas sensing behavior of $CuFeO_2$ delafossite type inorganic wires Fe and Cu complexes as single source molecular precursors, *RSC Adv.*, 2014, **4**, 15348.

3 C. G. Read, Y. Park and K.-S. Choi, Electrochemical synthesis of p-type $CuFeO_2$ electrodes for use in photoelectrochemical cell, *J. Phys. Chem. Lett.*, 2012, **14**, 1872.

4 A. P. Amurte, G. O. Larrazabal, C. Mondelli and J. Perez-Ramirez, $CuCrO_2$ delafossite: a stable copper catalyst for chlorine production, *Angew. Chem., Int. Ed.*, 2014, **4**, 15348.

5 C. L. Li, J. F. He, Y. Q. Xiao, Y. B. Li and J. J. Delaunary, Earth-abundant Cu-based metal oxide photocathodes for photoelectrochemical water splitting, *Energy Environ. Sci.*, 2020, **13**, 3269.

6 M. H. Dhaou, S. Hcini, A. Mallah, M. L. Bouazizi and A. Jemni, Structural and complex impedance spectroscopic studies of $Ni_{0.5}Mg_{0.3}Cu_{0.2}Fe_2O_4$ ferrite nanoparticle, *Appl. Phys. A*, 2017, **123**(8), 1–9.

7 P. Garcia-Munoz, F. Fresno, V. A. de la Pena O'Shea and N. Keller, Ferrite materials for photoassisted environmental and solar fuels applications, *Top. Curr. Chem.*, 2020, **378**(6), 1–43.

8 M. I. A. Abdel Maksoud, R. A. Fahim, A. E. Shalan, M. A. Elkodous, S. O. Olojede, A. I. Osman, C. Farrell, A. H. Al-Muhtaseb, A. S. Awed, A. H. Ashour and D. W. Rooney, Advanced materials and technologies for supercapacitors used in energy conversion and storage: a review, *Environ. Chem. Lett.*, 2021, **19**, 375.

9 R. Eivazzadeh-Keihan, S. Asgharnasl, M. S. Bani, F. Radinekiyan, A. Maleki, M. Mahdavi, P. Babaniamansour, H. Bahreinizad, A. E. Shalan and S. Lanceros-Mendez, Magnetic copper ferrite nanoparticles functionalized by aromatic polyamide chains for hyperthermia applications, *Langmuir*, 2021, **37**, 8847.

10 F. Ye, Y. Ren, Q. Huang, J. A. Fernandez-Baca, P. C. Dai, J. W. Lynn and T. Kimura, Spontaneous spin-lattice coupling in the geometrically frustrated triangular lattice antiferromagnet $CuFeO_2$, *Phys. Rev.B: Solid State*, 2006, **73**(R), 220404.

11 T. Kimura, J. C. Lashley and A. P. Ramirez, Inversion-symmetry breaking in the noncollinear magnetic phase of the triangular-lattice antiferromagnet $CuFeO_2$, *Phys. Rev.B: Solid State*, 2006, **73**(R), 220401.

12 L. Zhang, B. A. Goodman, D. K. Xiong and W. Deng, Magnetic transitions in delafossite $CuFeO_2$: a magnetocaloric effect study, *Phys. Lett. A*, 2019, **383**, 125834.

13 H. Schmid, Multi-ferroic magnetoelectric, *Ferroelectrics*, 1994, **162**, 317.

14 N. A. Hill, Why are there so few magnetic ferroelectrics?, *J. Phys. Chem. B*, 2000, **104**, 6694.

15 W. Eerenstein, N. D. Mathur and J. F. Scott, Multiferroic and magnetoelectric materials, *Nature (London)*, 2006, **442**, 759.

16 N. P. Salke, K. Kamali, T. R. Ravindran, G. Balakrishnan and R. Rao, Raman spectroscopic studies of $CuFeO_2$ at high pressure, *Vib. Spectrosc.*, 2015, **81**, 112.

17 S. P. Pavunny, A. Kumar and R. S. Katiyar, Raman spectroscopy and field emission characterization of delafossite $CuFeO_2$, *J. Appl. Phys.*, 2010, **107**, 013522.

18 O. Aktas, K. D. Truong, T. Otani, G. Balakrishnan, M. J. Clouter, T. Kimura and G. Quirion, Raman scattering study of delafossite magnetoelectric multiferroic compounds: $CuFeO_2$ and $CuCrO_2$, *J. Phys.: Condens. Matter*, 2012, **24**, 036003.

19 M. Roble, S. D. Rojas, R. Wheatley, S. Wallentowitz, A. L. Cabrera and D. E. Diaz-Droguett, Hydrothermal improvement for 3R-$CuFeO_2$ delafossite growth by control of mineralizer and reaction atmosphere, *J. Solid State Chem.*, 2019, **271**, 314.

20 R. A. Wheatley, S. Rojas, C. Oppolzer, T. Joshi, P. Borisov, D. Lederman and A. L. Cabrera, Comparative study of the structural and optical properties of epitaxial $CuFeO_2$ and $CuFe_{1-x}Ga_xO_2$ delafossite thin films grown by pulse laser deposition methods, *Thin Solid Film*, 2017, **626**, 110.

21 V. Eyert, R. Frésard and A. Maignan, Long-range magnetic order and spin-lattice coupling in delafossite $CuFeO_2$, *Phys. Rev.B: Solid State*, 2008, **78**, 052402.

22 N. Wolf, T. Schwaigert, D. Siche, D. G. Schlom and D. Klimm, Growth of $CuFeO_2$ single crystals by the optical floating-zone technique, *Appl. Phys. Lett.*, 2020, **535**, 125426.

23 G. J. Shu, *et al.*, Private communication.

24 D. M. Ginsberg, *Physical Properties of High Temperature Superconductors I* World Scientific, Singapore, 1989, p. 409.

25 H. W. Chen, Y. W. Chen, J. L. Kuo, Y. C. Lai, F. C. Chou, C. H. Du and H. L. Liu, Spin-charge-lattice coupling in $YBaCuFeO_5$: Optical properties and first-principles calculations, *Sci. Rep.*, 2019, **9**, 3223.

26 H. W. Chen, D. P. Gulo, Y. C. Chao and H. L. Liu, Characterizing temperature dependent optical properties of $(MA_{0.13}FA_{0.87})PbI_3$ single crystals using spectroscopic ellipsometry, *Sci. Rep.*, 2019, **9**, 3223.

27 C. M. Nelson, M. Spies, L. S. Abdallah, S. Zollner, Y. Xu and H. Luo, Dielectric function of $LaAlO_3$ from 0.8 to 6 eV between 77 and 700 K, *J. Vac. Sci. Technol., A*, 2012, **30**, 061404.

28 D. A. G. Bruggeman, Berechnung verschiedener physikalischer Konstanten von heterogenen Substanzen. I. Dielektrizitatskonstanten und Leitfahigkeiten der Mischkorper aus isotropen Substanzen, *Ann. Phys.*, 1935, **24**, 636.

© 2021 The Author(s). Published by the Royal Society of Chemistry

29 R. Kruger, B. Schulz, S. Naler, R. Rauer, D. Budelmann, J. Backstrom, K. H. Kim, S.-W. Cheong, V. Perebeinos and M. Rubhausen, Orbital ordering in $LaMnO_3$ investigated by resonance Raman spectroscopy, *Phys. Rev. Lett.*, 2004, **92**, 0927203.

30 L. Martin-Carron and A. de Andres, Excitations of the orbital order in $RMnO_3$ manganites: light scattering experiments, *Phys. Rev. Lett.*, 2004, **92**, 175501.

31 J. Andreasson, J. Holmlund, R. Rauer, M. Kall, L. Borjesson, C. S. Knee, A. K. Eriksson, S.-G. Eriksson, M. Rubhausen and R. P. Chaudhury, Electron-phonon interactions in perovskites containing Fe and Cr studied by Raman scattering using oxygen-isotope and cation substitution, *Phys. Rev.B: Solid State*, 2008, **78**, 235103.

32 J. Menendez and M. Cardona, Temperature dependence of the first-order Raman scattering by phonons in Si, Ge, and α–Sn: Anharmonic effects, *Phys. Rev.B: Solid State*, 1984, **29**, 2051.

33 T. Okuda, Y. Beppu, Y. Fujii, T. Onoe, N. Terada and S. Miyasaka, Specific heat of delafossite oxide $CuCr_{1-x}Mg_xO_2$, *Phys. Rev.B: Solid State*, 2008, **77**, 134423.

34 J. I. Pankove, *Optical Processes in Semiconductors* Dover, New York, 1971.

35 M. J. Pan and C. A. Randall, A brief introduction to ceramic capacitors, *IEEE Electr. Insul. Mag.*, 2010, **26**, 44.

36 K. P. O'Donnell and X. Chen, Temperature dependence of semiconductor band gaps, *Appl. Phys. Lett.*, 1991, **58**, 2924.

37 W. W. Li, J. J. Zhu, J. D. Wu, J. Gan, Z. G. Hu, M. Zhu and J. H. Chu, Temperature dependence of electronic transitions and optical properties in multiferroic $BiFeO_3$ nanocrystalline film determined from transmittance spectra, *Appl. Phys. Lett.*, 2010, **97**, 121102.

38 H. L. Liu, M. K. Lin, Y. R. Cai, C. K. Tung and Y. H. Chu, Strain modulated optical properties in $BiFeO_3$ thin films, *Appl. Phys. Lett.*, 2013, **103**, 181907.

39 P. K. Gogi and D. Schmidt, Temperature-dependent dielectric function of bulk $SrTiO_3$: Urbach tail, band edges, and excitonic effects, *Phys. Rev.B: Solid State*, 2016, **93**, 075204.

40 V. Železnỳ, D. Chvostová, D. Šimek, F. Máca, J. Mašek, N. Setter and Y. H. Huang, The variation of $PbTiO_3$ bandgap ferroelectric phase transition, *J. Phys.: Condens. Matter*, 2016, **28**, 025501.

41 H. Y. Huang, Z. Y. Chen, R.-P. Wang, F. M. F. de Groot, W. B. Wu, J. Okamoto, A. Singh, Z.-Y. Li, J.-S. Zhou, H.-T. Jeng, G. Y. Guo, Je-G. Park, L. H. Tjeng, C. T. Chen and D. J. Huang, Jahn-Teller distortion driven magnetic polarons in magnetite, *Nat. Commun.*, 2017, **8**, 15929.

42 L. Vina, S. Logothetidis and M. Cardona, Temperature dependence of the dielectric function of germanium, *Phys. Rev. B: Condens. Matter Mater. Phys.*, 1984, **30**, 1979.

© 2021 The Author(s). Published by the Royal Society of Chemistry